Title
Unraveling the CO Oxidation Mechanism over Highly Dispersed Pt Single Atom on Anatase TiO2 (101)

Journal
ACS Catalysis, 14(10)

ISSN
2155-5435

Authors
Tesvara, Celine
Yousuf, Raian
Albrahim, Malik
et al.

Publication Date
2024-05-17

DOI
10.1021/acscatal.4c01018

Unraveling the CO Oxidation Mechanism over Highly Dispersed Pt Single Atom on Anatase TiO_2 (101)

Celine Tesvara[a#], Md Raian Yousuf[b#], Malik Albrahim[c,b], Diego Troya[d], Abhijit Shrotri[f], Eli Stavitski[g], Ayman M. Karim[b]*, Philippe Sautet[a,e]*

[a]Department of Chemical and Biomolecular Engineering, University of California, Los Angeles, Los Angeles, CA 90095, USA

[b]Chemical Engineering Department, Virginia Polytechnic Institute and State University, Blacksburg, VA 24061, USA

[c]Department of Chemical Engineering, College of Engineering, University of Hail, Hail 55211, Saudi Arabia

[d]Department of Chemistry, Virginia Polytechnic Institute and State University, Blacksburg, VA 24061, USA

[e]Department of Chemistry and Biochemistry, University of California, Los Angeles, Los Angeles, CA 90095, USA

[f]Institute for Catalysis, Hokkaido University, Kita-Ku, Sapporo, Japan, 001-0021

[g]National Synchrotron Light Source II, Brookhaven National Laboratory, Upton, New York 11973, United States

*Corresponding Author: sautet@ucla.edu and amkarim@vt.edu

[#]These authors have equal contributions

Abstract

Catalysts with noble metals deposited as single atoms on metal oxide supports have recently been studied extensively due to their maximized metal utilization and potential for performing difficult chemical conversions owing to their unique electronic properties. Understanding of the reaction mechanisms on supported metal single atoms is still limited but is highly important for designing more efficient catalysts. In this study, we report the complexity of the CO oxidation reaction mechanism on Pt single atoms supported on anatase TiO_2 (Pt_{SA}/a-TiO_2) by coupling density functional theory (DFT) calculations and microkinetic analysis with kinetic measurements, *in situ/operando* infrared and X-ray absorption spectroscopies. Starting from the adsorbed Pt_{SA} occupying an O vacancy induced by reductive pretreatment, we show that CO oxidation follows a complex mechanism consisting of initiation steps to reorganize the active site and multi-branch reactive cycles, with the Pt_{SA}/a-TiO_2 catalyst not returning to its initial configuration. The initiation step consists of CO and O_2 adsorption healing the O vacancy, followed by CO oxidation using a gas-phase CO to form Pt(CO). The reactive cycle alternates O_2 adsorption and dissociation to oxidize the catalyst to Pt(O)(O)(CO) and branching pathways of competing Langmuir–Hinshelwood (LH) or Eley-Rideal (ER) type CO oxidation steps to reduce it again to Pt(CO). *In situ/operando* infrared experiments, including cryogenic CO adsorption and isotopic CO exchange, confirm the combined involvement of strongly adsorbed CO and of gas-phase CO in an Eley-Rideal step along the reaction cycle. Microkinetic modeling shows that Pt single atoms are present in a mixture of Pt(CO), Pt(CO)(O_2), Pt(O)(CO)(O_2), and Pt(CO)(CO_3) structures as main intermediates during steady-state CO oxidation, all having C-O vibrational stretch close to the experimentally observed value of 2115 cm^{-1}. Microkinetic modeling also shows that the fractional CO and O_2 orders measured experimentally originate from multiple steps with a high degree of rate control and not from a simple competitive adsorption. The results demonstrate the complex reaction pathways that even CO oxidation on a simple single-atom system can follow, providing mechanistic insights for designing efficient Pt-based single-atom catalysts. We further show that microkinetic modeling results are sensitive to changes in energies of intermediate and transition states within errors of density functional theory, which can ultimately lead to incorrect conclusions regarding the reaction pathways and most abundant reaction intermediates if not accounted for by experiments.

Keywords: single-atoms catalysts, CO oxidation, reaction mechanism, microkinetic modeling, *in situ/operando* spectroscopy, density functional theory (DFT), reaction kinetics

Introduction

Pt group metals (PGM) are widely used in many industrial catalytic processes. However, their expense and scarcity led to much attention and effort towards singly dispersed supported metal atoms as these systems provide maximum metal utilization, well-defined active sites, and in some cases improved catalytic efficiency. Moreover, metal single atoms offer unique electronic properties due to unsaturated coordination environment and better access to frontier orbitals for interaction with the support atoms, which allows for chemical transformations that would otherwise be difficult[1–13]. To utilize the full potential of the single-atom catalysts, however, it is important to understand structure-activity relations and to obtain mechanistic insights for the relevant reaction.

As Pt is an important catalyst for many industrial applications, including CO oxidation for automobile pollution control, Pt single-atom (Pt_{SA}) catalysts have been investigated extensively in recent years[3,7–10,12–16]. Amongst metal oxide supports for single atom catalysts, titanium dioxide (TiO_2; Titania) has been gaining popularity due to its affordability, ease of access, and established routes of synthesis in the literature[17,18]. Titania exists in three crystal structures, namely anatase, brookite and rutile at temperatures below 500 °C [19–22]. There are not many studies on brookite itself as support for single atoms, not only because it is a metastable phase, but also because it is difficult to synthesize[23]. Due to its higher surface area and less constrained structure, anatase is often found to be the common product phase during the synthesis of titania[24]. Although both rutile and anatase can anchor metal single atoms, the synthesis of supported single atoms on anatase TiO_2 is more accessible and has already been performed[14,25,26]. The ease of synthesis, stability at low temperatures, and ability to stabilize single atoms make anatase TiO_2 an ideal candidate as a metal single atom catalyst support.

Despite Titania's ability to stabilize single metal atoms, the determination of their stability and intrinsic reactivity under operating reaction conditions is intricate due to the heterogeneity in the local coordination of these active metal sites and the dynamic changes in their coordination under different chemical environment and reaction conditions[14,27–30]. A combined experimental (Fourier-transform infrared spectroscopy (FTIR), scanning transmission electron microscopy (STEM), and X-ray photoelectron spectroscopy (XPS)) and theoretical (density functional theory (DFT)) study on Rh single-atom catalyst (SAC) on rutile TiO_2(110) showed that Rh may adapt its adsorption site and coordination depending on the gas pretreatment condition[28]. In oxidative conditions, Rh may substitute the surface Ti_{5c} (five-fold coordinated Ti), whereas in reducing conditions, Rh prefers to be supported on the surface instead of substituting Ti. A recent work by DeRita *et al.*[14] on TiO_2-supported Pt single atoms showed that Pt can be deposited as stable isolated atoms on

anatase TiO_2 nanoparticles under various pretreatment conditions: oxidative (300 °C in 100% O_2), mild reduction (250 °C in 10% H_2) and harsh reduction (450 °C in 10% H_2). Interestingly, it was shown that the local coordination and oxidation/charge state of Pt single-atom species depend on these pretreatment conditions, which in turn impact the stability and activity of the supported Pt atoms. For instance, 300 °C oxidation, 250 °C reduction or 450 °C reduction resulted in Pt substituting six-fold coordinated Ti, adsorbed Pt(O_2) species, or adsorbed Pt(OH) species, respectively. The Pt atoms remained isolated in all cases with the Pt(OH) species being mobile and adsorbed on both step and terrace sites. In another recent study, Thompson *et al.*[31] showed that Ir SA is adsorbed/supported on anatase TiO_2 after CO reduction pretreatment with a *gem*-dicarbonyl ligand environment and binding to two lattice O from TiO_2. Under CO oxidation atmosphere, the Ir SA ligand environment changes where Ir is coordinated to one CO (monocarbonyl), one lattice O, and two other O from gas-phase O_2 dissociation.

The dynamic nature of SA Pt species during catalyst pretreatment and under reaction environment makes it challenging to describe the catalytic activity of highly dispersed single atoms in a level that connects to the characterization of the local geometric structure (resting state) from experiment alone. This is more so because evolution of the local coordination of these isolated Pt species during CO oxidation, *i.e.* the evolution through the reaction cycle is difficult to follow experimentally unless more than one intermediate can be isolated[31]. Moreover, although the structural details of the isolated Pt sites, their dynamic response to pretreatment environments causing difference in local coordination, and its influence on chemical reactivity have been studied by DeRita *et al.* [14], the origin of their activity and reaction kinetics, rate-determining intermediates, and detailed reaction pathways and mechanism are still missing. It is important to understand these details for achieving guiding principles so that active and efficient Pt catalysts consisting of isolated single atoms can be designed in the future.

Additionally, it is crucial to understand what role oxygen atoms from the TiO_2 lattice play in the CO oxidation mechanism, given that TiO_2 is a reducible support. This will allow for optimal selection and tuning of support for single-atom Pt group catalysts. Previously, it has been reported for CeO_2-supported Pt nanoparticles that reactive and mobile/labile support lattice oxygen (O*) can be supplied by the interfacial sites at the Pt-CeO_2 interface, where labile/reactive O* can travel from distance to react with the adsorbed CO at the interfacial Pt sites, thus enhancing CO oxidation reactivity[32,33]. However, the involvement of reactive labile lattice oxygen for CO oxidation on TiO_2-supported Pt single-atom is still unknown.

In this work, we describe the dynamic structure of stable and uniform Pt single atoms (Pt_{SA} hereafter) deposited on the surface of anatase TiO_2, their reactivity towards CO oxidation, and the detailed mechanism of the reaction by combining experimental methods (DRIFTS, STEM, X-ray absorption spectroscopy (XAS) and kinetic studies) and computational approaches from first principles (DFT and microkinetic modeling). We studied the local coordination environment of the Pt single atoms and the CO adsorption behavior on these isolated sites after reduction and during CO oxidation to identify the rate-controlling intermediate(s) and step(s). We show that the starting catalyst after reduction is a supported (adsorbed) Pt atom on anatase-TiO_2 (101) with one oxygen vacancy ($Pt_{ads}O_{vac1}$). Upon exposure to CO and O_2 it turns into Pt(CO) without O vacancy, and initiates the reaction cycle with competing branching pathways involving Langmuir–Hinshelwood (LH) or Eley-Rideal (ER) type CO oxidation. We demonstrate that the first chemisorbed CO generally binds strongly on Pt and that a second gas-phase CO can be involved favorably in the reaction resulting in the experimentally observed Eley-Rideal step. Furthermore, microkinetic modelling reveals that the fractional CO and O_2 reaction orders originate from multiple competing rate-determining intermediates and transition states. These results demonstrate that CO oxidation may undergo multi-branch convoluted reaction pathways even on a simple supported single-atom system.

Results and Discussion

Synthesis, Structure, and Stability of Pt_{SA}/a-TiO_2

We confirm the presence and the stability of isolated Pt atoms on anatase TiO_2 using *ex situ* microscopy and *in situ* DRIFTS. *Ex situ* aberration-corrected high-angle annular dark-field scanning transmission electron microscopy (AC-HAADF-STEM) images collected after CO oxidation kinetics experiments (in **Figure 1** (a) and **Figure S4**) show singly dispersed Pt atoms (enclosed in dashed pink circles) on the TiO_2 surface even after enduring the high-temperature reduction pretreatment (350 °C) and prolonged reaction gas environment (after ~18 hours of CO oxidation kinetics measurement at 160 °C). *In situ* CO adsorption DRIFTS at 35 °C on the H_2-reduced state shows a symmetric peak at ~2073 cm^{-1} (**Figure 1** (b)) in the ν_{CO} region corresponding to the C-O vibrational frequency on the reduced Pt_{SA}. However, the peak is somewhat broad (full width at half maximum, FWHM of 32 cm^{-1}) indicating some inhomogeneity in the local environment around the Pt_{SA} sites. The 2073 cm^{-1} peak observed experimentally matches the DFT-calculated frequency for the most stable adsorbed structure of the Pt_{SA} under these conditions (2065 cm^{-1}; structure labelled "$Pt_{ads}O_{vac1}$" in **Figure 1** (c)). This suggests consistency between the synthesized Pt_{SA} species and the modeled Pt_{SA}/a-TiO_2(101) species. An almost identical CO chemisorption peak was obtained after regenerating the catalyst following CO oxidation, showing the stable nature of the Pt_{SA}/a-TiO_2 catalyst (see **Figure S5**). Thus, STEM and DRIFTS show that Pt stays as single-atom species supported on anatase TiO_2 during CO oxidation. Our DFT calculations and *in situ* DRIFTS show that Pt_{SA}/a-TiO_2 can adopt different configurations depending on pretreatment condition and gas environment. **Figure 1** (d) shows the sensitivity of the Pt_{SA}/a-TiO_2 (101) structure on the condition prior to CO exposure. In reducing conditions, Pt_{SA} is most stable as supported on the two-fold-coordinated surface oxygen (O_{2c}) vacancy sites formed on a-TiO_2 (structure "$Pt_{ads}O_{vac1}$" in **Figure 1** (c)). As discussed earlier, the measured C-O vibrational frequency on the reduced Pt_{SA} species was 2073 cm^{-1} which matches well with the DFT-calculated frequency of 2065 cm^{-1} corresponding to Pt adsorbed on TiO_2 with one O vacancy sites (structure "$Pt_{ads}O_{vac1}$" in **Figure 1** (c), (d), and **Figure S6** (a)). This state represents the initial reduced state of the catalyst before exposing it to the oxidizing reaction environment, *i.e.* CO + O_2 flow. In contrast, in oxidizing conditions under O_2 (high oxygen chemical potential; right-hand side of the stability diagram in **Figure 1** (d)), the most stable species corresponds to Pt_{SA} substituting a six-fold-coordinated Ti sites (structure "Pt_{subTi}" in **Figure 1** (d) and **Figure S6** (a)). The behavior of Pt_{SA} substituting the Ti cation as dopant has been seen before on rutile TiO_2. Tang *et al.*[28] showed a thermodynamic analysis on rutile TiO_2 where Rh prefers to

substitute the bridging Ti_{6c} (six-fold-coordinated Ti) sites. Meanwhile, a combined FTIR and DFT work by Thang *et al*. suggested that Pt_{SA} most likely adopts the supported/adsorbed structure[26,27]. However, a follow up work by DeRita *et al.* confirmed the dynamic nature of Pt_{SA}: substituted Pt on six-fold-coordinated Ti (Ti_{6c}) site upon oxidation conditions and supported/adsorbed $Pt_{ads}O_2$ species after mild reduction[14]. Since the catalyst in this study undergoes reduction prior to CO oxidation, the subsequent DFT modeling of the reaction pathways follows the reduced "$Pt_{ads}O_{vac1}$" structure, as per agreement found by DRIFTS and DFT-calculated C-O vibrational frequency.

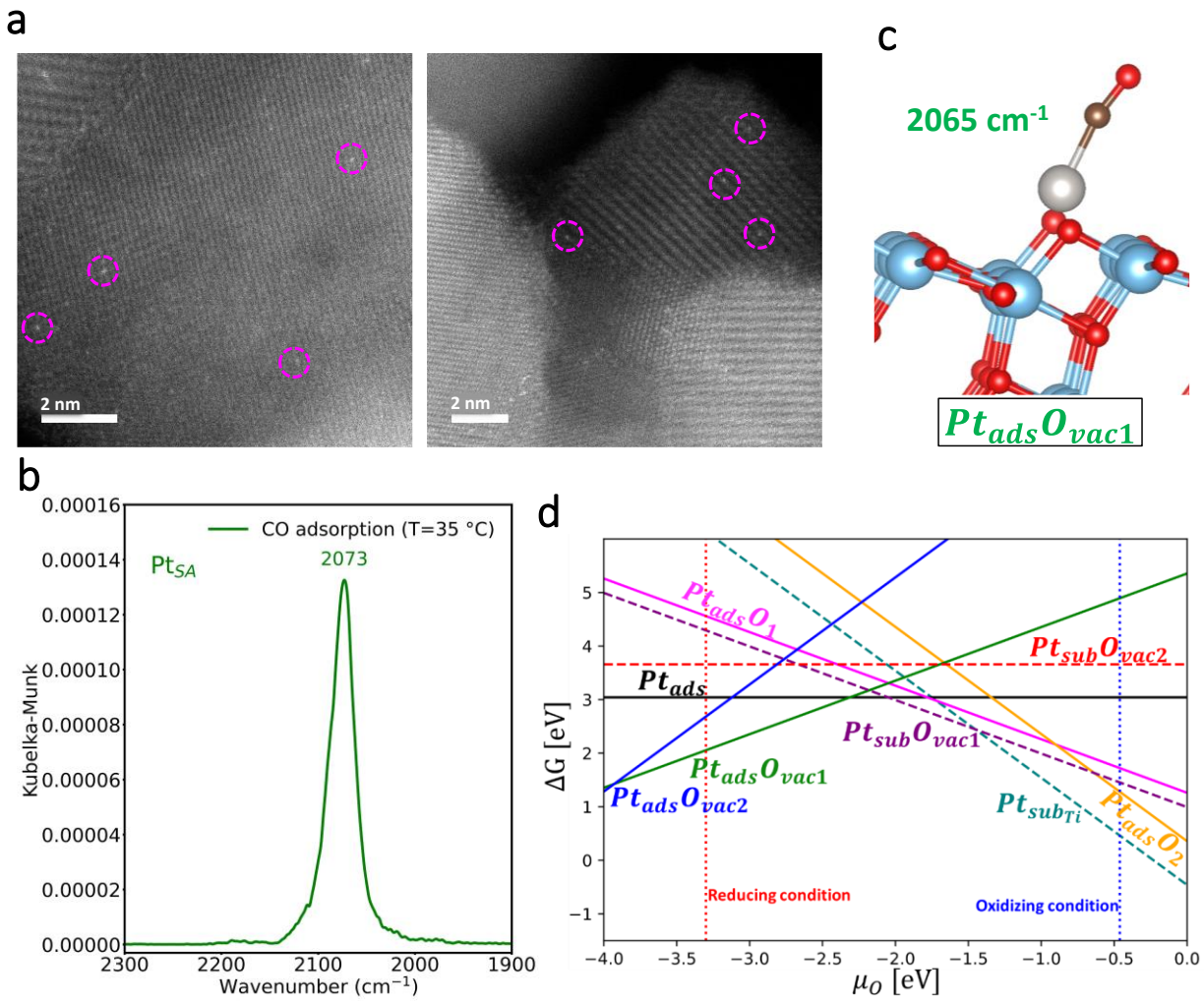

Figure 1: (a) *Ex situ* AC-HAADF-STEM images of the Pt_{SA}/a-TiO_2 sample taken after the reduced sample went through the CO oxidation kinetic experiment, showing the singly dispersed Pt atoms as enclosed in pink circles. **(b)** *In situ* DRIFTS spectra of CO adsorption at 35 °C after H_2 reduction pretreatment. H_2 reduction pretreatment was performed at 350 °C for 2 hr. **(c)** Calculated structure and vibrational frequency of CO adsorbed on Pt_{SA}/a-TiO_2(101) which corresponds to the reduced state of the catalyst and the starting catalyst for the CO oxidation cycle. The frequency value agrees well with the DRIFTS spectrum in **Figure 1** (b). **(d)** Stability diagram of the different configurations of the supported Pt_{SA} on anatase TiO_2(101) under different gas environments (please see **Figure S6** (a) for all structures).

To further understand how CO would affect the stability of Pt_{SA}/a-TiO_2(101), a similar study was conducted with the presence of CO absorbed on all the Pt_{SA} species, with the CO chemical potential corresponding to the conditions P_{CO} = 1 kPa and T = 25 °C. Upon exposure to CO, Pt(CO) structure on the pristine TiO_2 surface where Pt is supported/adsorbed on TiO_2 ("Pt_{ads}" structure in **Figure S6** (b)) becomes the most stable configuration in a large range of reducing condition oxygen chemical potential, while in oxidizing conditions, Pt substituting Ti_{6c} ("Pt_{subTi}" structure in **Figure S6** (b)) is still the most thermodynamically stable species followed by the metastable supported/adsorbed "$Pt_{ads}O_2$" structure (see structures in **Figure S6** (b)). The crossing in stability between the Ti-substituting Pt_{SA} and the supported Pt_{SA} now occurs at a much higher chemical potential (-0.9 eV, compared to -1.75 eV prior to CO exposure). Therefore, the interactions between CO and Pt decrease the thermodynamic driving force for restructuring the Pt atom from adsorbed to substituted in oxidizing conditions.

Elucidation of CO Oxidation Pathway and Active Species

The oxidation pathways of CO and its Gibbs free energy diagram were explored using DFT at experimental conditions (T = 160 °C, P_{CO}= 1 kPa, P_{O_2}= 10 kPa) and 5% conversion (**Figure 2** (a) and (b), respectively). The supported/adsorbed $Pt_{ads}O_{vac1}$ structure was the starting configuration (structure I in **Figure 1** (c) and **Figure 2** (a)). Calculations show that the reaction consists of an initiation step and a reactive cycle where the system does not return to the initial catalyst configuration. The initiation step consists of CO and O_2 adsorption on structure I, followed by an Eley-Rideal (ER) type CO oxidation using a gas-phase CO to ultimately form Pt(CO) (structure IV in **Figure 2** (a)). The initiation step is very facile as the adsorbing O_2 heals the vacancy and provides a reactive O adatom, resulting in a large thermodynamic driving force and a small barrier to form CO_2 even at room temperature via the E-R mechanism (**Figure 2** (b)). This is shown experimentally as the fresh reduced Pt_{SA} catalyst with a CO vibrational frequency of 2073 cm^{-1} gets oxidized when exposed to O_2 (**Figure 3** (a)) and the CO peak blueshifts from 2073 cm^{-1} to two peaks positioned at 2087 and 2115 cm^{-1} upon O_2 flow. Upon CO re-adsorption the intensity of both peaks increases, indicating a role of both CO and O_2 in the initiation cycle. Notably, the co-flow, or reversing the order of CO and O_2 flow at 35 °C on the reduced Pt_{SA} state also led to the same two peaks with similar intensity (**Figure S9**(a)). These two peaks, positioned at 2087 and 2115 cm^{-1}, merge into a single peak positioned at 2115 cm^{-1} in the initial stages of heating the catalyst (**Figure S9**(b)), which is the same peak observed under steady-state at 160 °C (**Figure 3** (b)), and suggests that the initiation step is facile, in agreement with the DFT-calculated initiation pathway in **Figure 2**. Furthermore, the CO-Pt peaks obtained experimentally (DRIFTS)

upon exposure to O_2 followed by CO or CO and O_2 co-flow on the reduced Pt_{SA} agree well with DFT-calculated vibrational frequencies of the states in the initiation cycle. Specifically, upon O_2 healing the O vacancy, the frequency shifted from 2065 cm^{-1} (experimental 2073 cm^{-1}) (starting CO-$Pt_{ads}O_{vac1}$ structure) to 2081 cm^{-1} (structure II in **Table S3**), forming an adsorbed Pt(O)(CO) species (structure II in **Figure 2** (a)). Finally, flowing CO leads to CO_2 formation via an Eley-Rideal step and results in the formation of structure IV with a calculated CO vibrational frequency of 2106 cm^{-1}, all in very good agreement with the experimental results in **Figure 3** (a). Importantly, the Pt_{SA} remains in the same state as in **Figure 3** (b) when cooled to room temperature (**Figure S9** (c); red spectrum) indicating that this is an irreversible initiation cycle. As will be discussed below, this is further shown by our calculations as well.

In summary, the initiation pathway starts with structure I and results in a reduced Pt(CO) species without O vacancy (intermediate IV, **Figure 2** (a)). From this Pt(CO) species (intermediate IV), the release of CO_2 via the Mars-van Krevelen (MvK) mechanism involving an O atom from theTiO_2 support is calculated to be uphill by 1.19 eV in Gibbs free energy, and thus unlikely to happen. This is further confirmed by isotopic $^{18}O_2$-$^{16}O_2$ switching during steady-state CO oxidation (**Figure S8**). We find that there was no CO_2 formation that involved adsorbed CO reacting with lattice ^{16}O from TiO_2, *i.e.* MvK mechanism, and all the CO_2 formation was due to reaction between adsorbed and/or gas-phase CO and adsorbed ^{18}O on Pt. However, the reaction can continue via O_2 adsorption in an η^2-manner on Pt (intermediate V). The dissociation of this O_2 results in intermediate VI (Pt(O)(O)(CO)). From intermediate VI, two possible pathways arise: the formation of CO_2 via an LH mechanism (black path) that results in the reduced Pt(O) intermediate (structure VIIIa) or via an ER mechanism involving an additional CO from gas phase, which is prone to formation of carbonate (red path, structure VIIIb). Carbonate formation during CO oxidation has been observed from experiment via DRIFTS (**Figure S10**), supporting this red ER pathway. Both pathways form a Pt(O) species with adsorbed CO (Pt(CO)(O), intermediate IX) upon adsorption of CO (VIIIa-IX, black path) or release of CO_2 (VIIIb-IX, red path).

From this Pt(CO)(O) species (structure IX), the reaction can continue via O_2 adsorption in a bridging manner between Pt and Ti, immediately followed by an Eley-Rideal CO oxidation from the gas phase CO to form CO_2 with the remaining O adatom (O_{ad}) of Pt(O)(CO)(O_2) (intermediate Xa, blue path). The barrier along this blue pathway is +0.58 eV (TS IIIa-IV). The release of CO_2 yields an isomer of intermediate V - the Pt(CO)(O_2) species (intermediate XIIa). Rearrangement of Pt(CO)(O_2) to a more stable isomer is facile via desorption and re-adsorption of O_2 (XIIa-IV-V). Alternatively, the Pt(CO)(O) species can absorb another CO (intermediate Xb, black path). This

path is only limited by the CO adsorption barrier (0.46 eV) and will initiate a LH type mechanism for the second CO_2 formation. The barrier to form CO_2 from intermediate Xb [Pt(CO)(CO)(O)] is very low (0.14 eV, TS IIIb), and the subsequent release of CO_2 regenerates the initial Pt(CO) structure (intermediate IV). From Pt(CO)(O) (IX) the direct formation of a CO_2 product is not favorable, since it leaves a bare Pt atom, a structure with high energy and low stability and not observed experimentally by DRIFTS (**Figure S9** and **S11**). We note that Pt_{SA} does not return to state I, confirming that the catalyst changes irreversibly after the initiation cycle as was seen from experiment as well (**Figure S9**).

It is interesting to note that both the initiation steps and the reactive pathway do not involve lattice oxygen of TiO_2 since all the pathways involve either an Eley-Rideal or Langmuir Hinshelwood type of mechanism with an O adatom on Pt. This behavior has recently been shown with other TiO_2 supported SAC. A work by Liu *et al.* showcased the CO oxidation kinetics on Ir_1/TiO_2 to follow mostly an Eley-Rideal mechanism and not Mars-van Krevelen mechanism that would involve oxygens from TiO_2 lattice.[31,34]

For what concerns the presence of oxygen vacancies on the pristine TiO_2 surface in reducing conditions, such vacancy sites on anatase (101) are known to be in the subsurface/bulk[35,36]. Exposure to oxygen has been found to attract these vacancies to the surface, with the O_2 species adsorbing flat on the O_{2c} vacancy sites. This adsorbed O_2 is reactive and may undergo an ER mechanism to create a CO_2 and a defect-free surface. However, this is a stoichiometric process and does not create a catalytic active site since the following MvK mechanism on pristine anatase was found to be endothermic by 1.29 eV in the literature, due to the high cost to create an oxygen vacancy in oxidation conditions[37–39].

Our mechanistic exploration shows a rich complexity of pathways involving different branches with similar barriers. Determining the favored path is therefore not directly possible from the reaction profile and requires microkinetic modeling as will be discussed below.

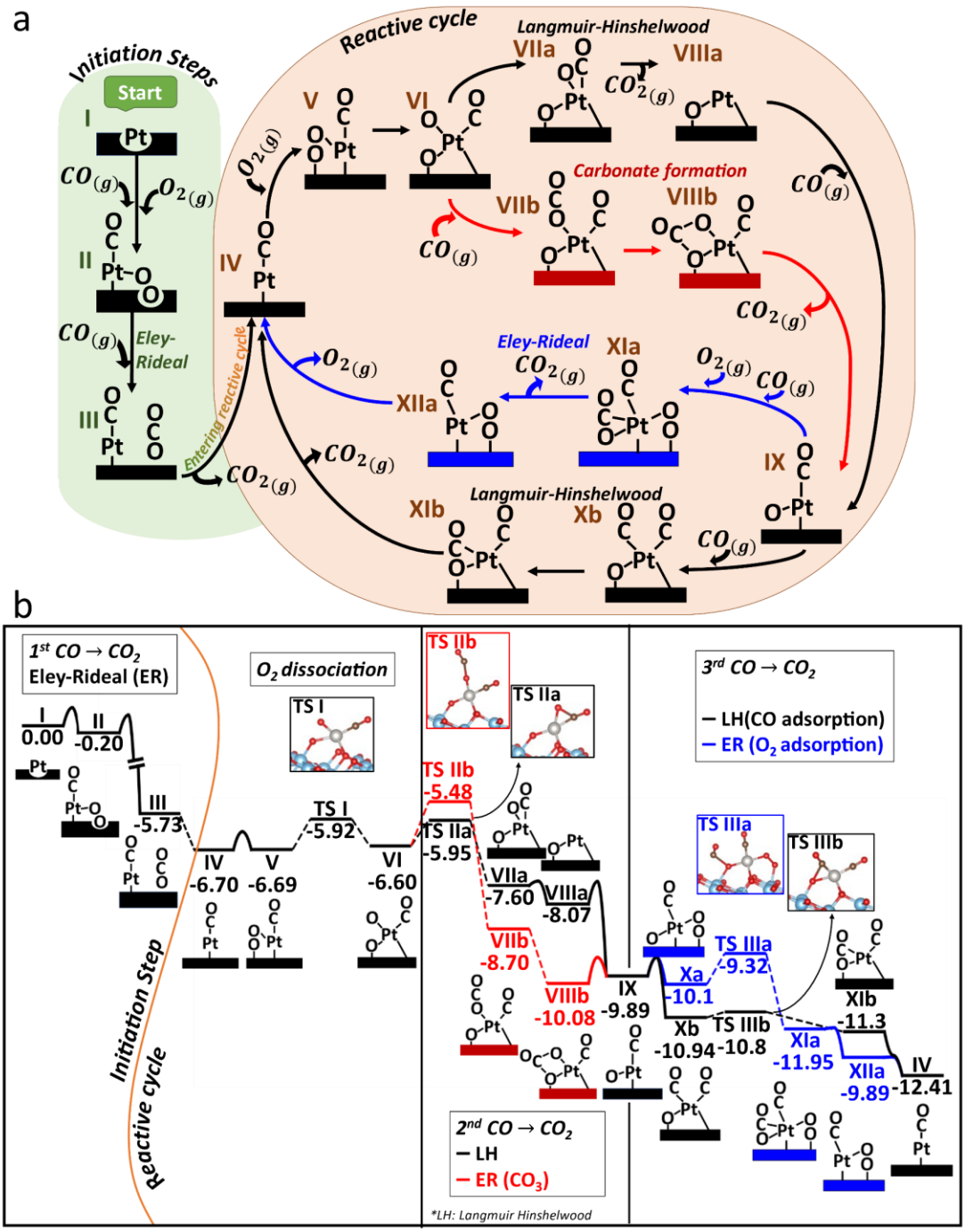

Figure 2: (a) The reaction pathway for CO oxidation on Pt_{SA}/a-TiO_2 (101) and **(b)** its respective Gibbs free energy landscape at reaction conditions (T = 160 °C, P_{CO}=1 kPa, P_{O2}=10 kPa, conversion = 5%). Surfaces with an O vacancy are represented by an inward concave. The reaction pathway consists of an initiation step and a catalytic reactive cycle. Elementary steps involving adsorption or desorption processes are connected with solid lines, indicating their respective adsorption free energy barrier. For elementary

reaction steps, transition state energy levels are explicitly indicated (labeled TS X) and linked by dashed lines. The structures of each intermediate are reported in more details in SI **Figure S7.**

Kinetics of CO oxidation: Microkinetic Analysis

Microkinetic Modeling (MKM) was employed to further understand the kinetics of CO oxidation on Pt_{SA}/a-TiO_2(101). As the system does not return to the initial $Pt_{ads}O_{vac1}$ structure (intermediate I) at steady-state, the microkinetic modeling was built on elementary reaction steps which describe the reactive cycle only. A list of elementary reaction steps describing the reactive cycle was built for the microkinetic analysis (**Table S2**). The MKM employed Gibbs free energies at experimental reaction conditions (T = 160 °C, P_{CO} = 1 kPa, P_{O2} = 10 kPa, conversion = 5%). Details of the MKM setup are listed in the supporting information (**Table S2** and associated discussion).

The MKM was run towards steady state. The most abundant intermediates on the surface were Pt(CO) (structure IV, 35.5%), Pt(O_2)(CO) (structure V, 26.8%), Pt(CO)(CO_3) (structure VIIIb, 19.6%), and Pt(O)(O_2)(CO) (structure Xa, 16.8%) (all shown in **Figure 3** (d)). We note here that intermediates IV and V are the most abundant species under steady-state and have CO vibrational frequencies of 2106 and 2116 cm^{-1}, respectively, providing a detailed interpretation of the CO vibrational frequency of 2115 cm^{-1} that we experimentally observe during steady-state CO oxidation at 160 °C (**Figure 3** (b)). Under CO and O_2 flow, species VIIIb and Xa were not observed as distinct peaks in DRIFTS (**Figure 3** (b)) likely due to their small contribution and their CO vibrational frequency (2137 and 2156 cm^{-1}, respectively; **Table S3**) falling in the same range as the large gas-phase CO peak and CO on Ti^{4+} peak. However, once the gas-phase CO and O_2 are purged, we observe a shoulder peak at 2159 cm^{-1} that matches well with the calculated frequency of 2156 cm^{-1} for species Xa. It is important to note that the chemisorbed CO observed during steady-state CO oxidation is bound strongly as observed experimentally from temperature-programmed desorption (TPD) of this species. The estimated binding energy was ~140 kJ/mol (see **Figure S13**, **Table S5**, and associated discussion for TPD procedure and analysis). This high binding energy is consistent with the fact that the 2115 cm^{-1} peak did not disappear and maintained a constant intensity even after flushing/purging with N_2 at 160 °C (**Figure 3** (b)).

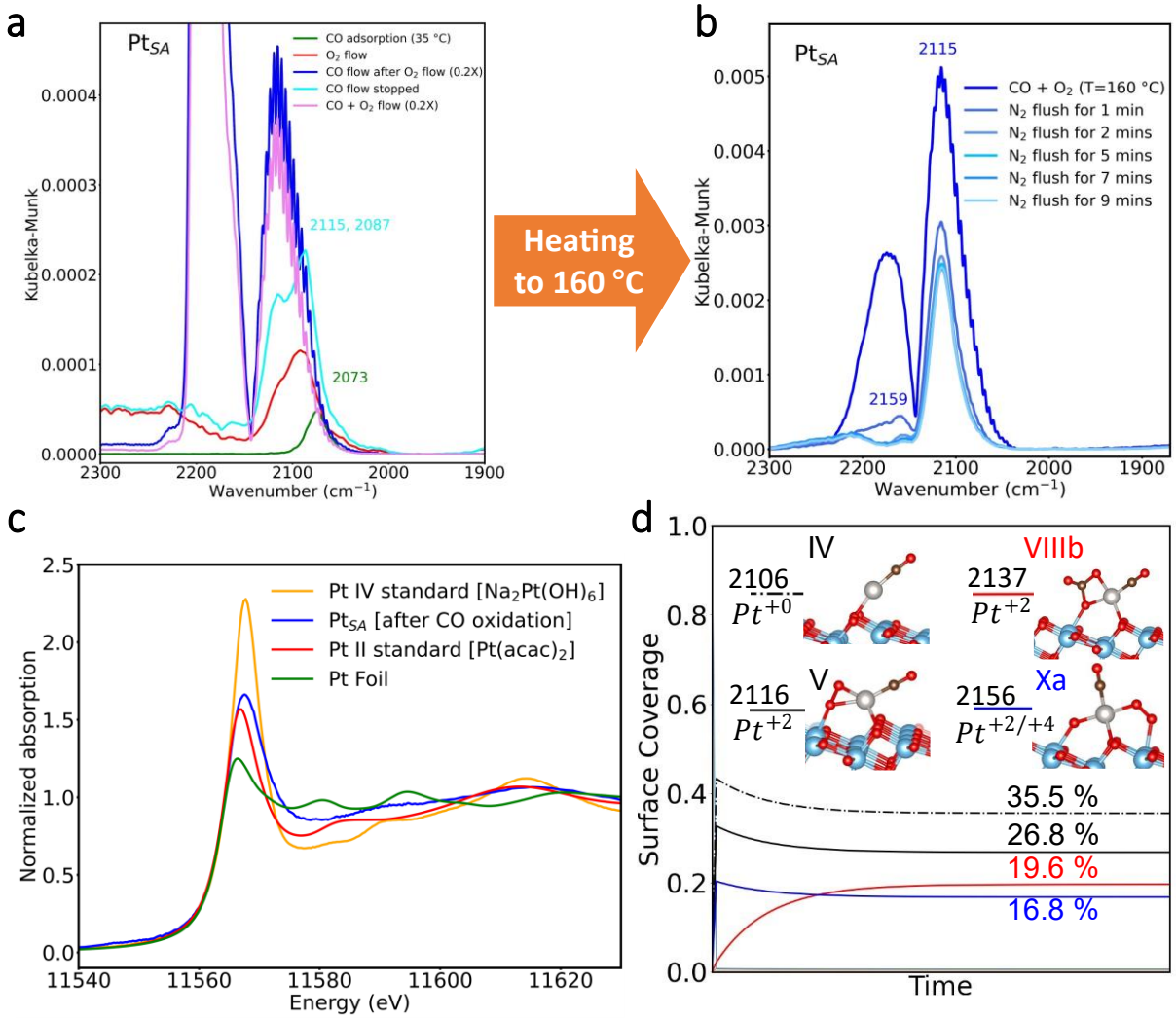

Figure 3: *In situ/operando* CO adsorption DRIFTS spectra for $Pt_{SA}/a\text{-}TiO_2$ **(a)** under different gas environments at 35 °C on the H_2 reduced state and **(b)** during CO oxidation at 160 °C and under different duration of N_2 flush of the reaction gas environment afterwards. **(c)** The white line intensity (WLI) region of the *in situ* XANES spectra for Pt_{SA} after CO oxidation compared against three standards – Pt foil, Pt^{2+}, and Pt^{4+}. **(d)** Surface coverage along the MKM simulations for the primary $Pt_{SA}/a\text{-}TiO_2$ species present during CO oxidation. In the legend, we indicate the corresponding CO vibrational frequency in cm^{-1} (above the line) and the formal Pt oxidation state derived from the Bader charge analysis (below the line; see **Table S4** for more details).

The MKM ensemble of surface species with significant coverage is consistent with the Gibbs free energy landscape, which suggests that there are few competing turnover frequency-determining intermediates (TDI), particularly intermediates IV and V. To estimate the oxidation state of the Pt_{SA} species, we performed *in situ* XAS at 35 °C after CO oxidation at 160 °C and compared the XANES white line intensity region against that of Pt foil, Pt II [$Pt(acac)_2$], and Pt IV [$Na_2Pt(OH)_6$]

standards (**Figure 3** (c)). It is evident from the similar white line intensity of the Pt_{SA} and $Pt(acac)_2$ that the Pt_{SA} species after CO oxidation is close to Pt^{2+}. From Bader charge analysis (**Table S4**), the Pt oxidation state (**Figure 3** (d)) of the most abundant intermediates (structure IV and V) during steady-state CO oxidation (at 160 °C) were found to be 0 and +2 (Bader charge 0.16 and 0.82, respectively; see **Table S3-S4** for details), respectively. To be consistent with the conditions of the XANES measurements, we ran microkinetic modeling of the CO oxidation at 27 °C and found that structure V ($Pt(O_2)(CO)$) is more stable and hence more probable than structure IV. Therefore, a Pt oxidation number of +2 is predicted by simulations under conditions similar to the experimental XANES measurements, suggesting consistency with the experimentally observed oxidation state.

CO oxidation rate measurements under strict kinetic control (**Figure 4** (a) and (b)) show apparent activation energy of 69±2 kJ/mol and fractional CO and O_2 reaction orders of 0.55±0.15 and 0.36±0.10, respectively. The reaction orders obtained from MKM are 0.24 and 0.46 for CO and O_2, respectively, qualitatively agreeing with the experimental values.

The turnover frequency (TOF) at 160 °C obtained from MKM on the other hand is significantly overestimated at 3.3×10^{3} (mol CO_2).(mol surface Pt)$^{-1}$.s^{-1}, compared to the experimental value of 3.8×10^{-3} (mol CO_2).(mol surface Pt)$^{-1}$.s^{-1}, indicating that the DFT calculation underestimated barriers in the reaction network, which is a general behavior.[34,40–42]This is also reflected in the calculated apparent activation energy of 45 kJ/mol compared to the experimental value of 69±2 kJ/mol. A summary of the computational and experimental CO oxidation kinetics is presented in **Table 1**.

Table 1: Turnover frequency (TOF), CO and O_2 reaction orders, and apparent activation energy (E_{app}) obtained from microkinetic modeling under experimental conditions and from experimental kinetic measurements. TOF, CO order, and O_2 order values are at 160 °C and apparent activation energy was measured between 150 and 170 °C.

Kinetic parameter	Value obtained from MKM	Value obtained from experiment
TOF (1/s)	3.3×10^{3}	3.8×10^{-3}
CO order	0.24	0.55±0.15
O_2 order	0.46	0.36±0.10
E_{app} (kJ/mol)	45	69±2

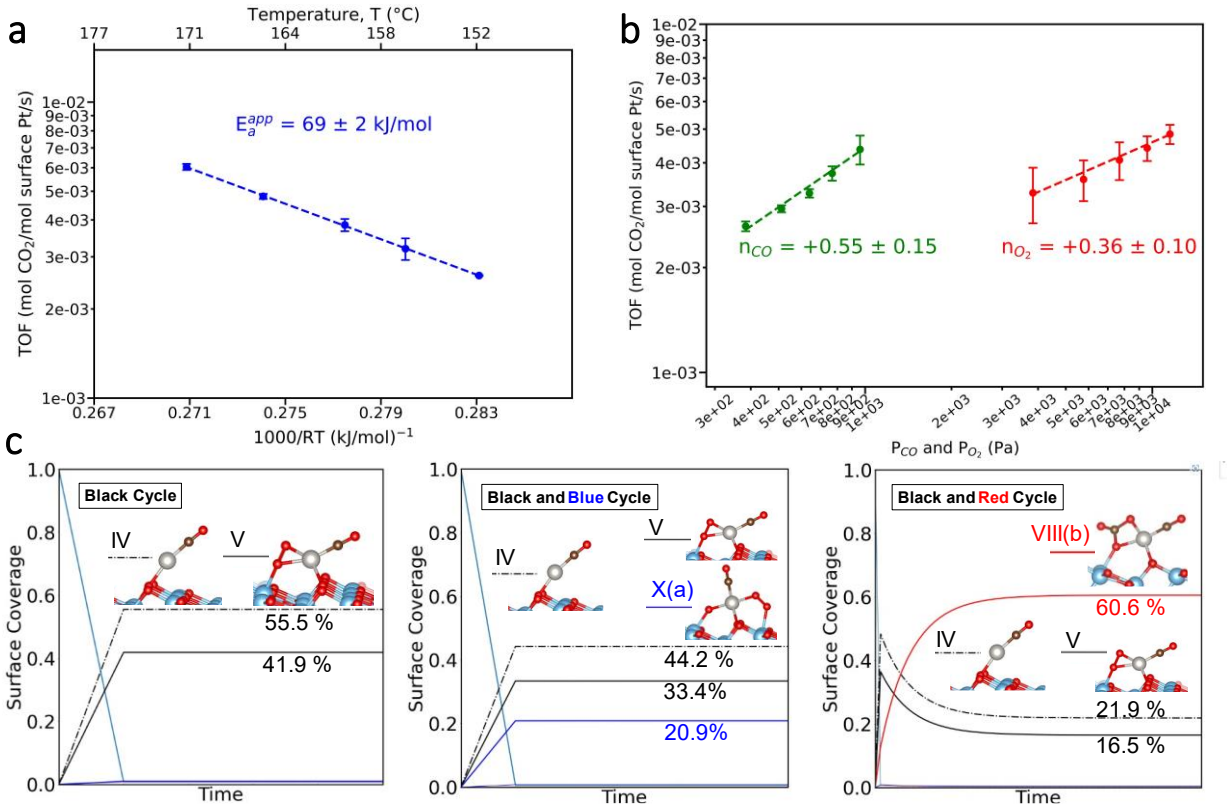

Figure 4: CO oxidation kinetic measurements on Pt_{SA}/a-TiO_2 with turnover frequency (TOF) calculated considering 100% Pt atoms are singly dispersed, *i.e.* on the surface. **(a)** Arrhenius plot (TOF vs 1000/RT) with the calculated apparent activation energy (E_{app}) value. E_{app} was measured between 150 and 170 °C with 1 kPa CO, 10 kPa O_2, and balance He to atmospheric pressure at 75 sccm total flow rate. **(b)** Effect of CO and O_2 partial pressure on TOF at 160 °C. Gas flow conditions: 0.4-1 kPa CO and 10 kPa O_2 for the effect of CO partial pressure; 1 kPa CO and 4-12 kPa O_2 for the effect of O_2 partial pressure with balance He to atmospheric pressure at 75 sccm total flow rate. **(c)** Surface coverage for model kinetic simulations including only part of the reaction pathways shown in **Figure 2** ("black", "black + blue", and "black + red" paths following colors of **Figure 2**) and corresponding majority structures.

On supported nanoparticles, fractional orders indicate competitive adsorption of CO and O_2 on the metal and/or a two-site mechanism where CO adsorption proceeds on the metal site while O_2 activation proceeds on the metal-support interface. However, on supported single atom catalysts the reaction pathway can be more complex due to the ability to adsorb more than one molecule at the same time as shown above (**Figure 2**) and can involve more than one kinetically relevant step.[31,34] Therefore, a detailed discussion of the experimental and simulated kinetics requires the computation of the TOF-determining transition states (TDTS), obtained with a degree of rate control (DRC) analysis[43] (shown in **Table 2**). Several TDTS are obtained along the branches of the pathway. The greatest DRC (0.45) is obtained for the O_2 dissociation step along the black

pathway (V-TSI-VI). However, the second Eley-Rideal CO_2 formation along the blue pathway (Xa-TSIIIa-XIa) also provides a significant DRC (0.24), together with the first CO_2 formation along the black pathway (VI-TSIIa-VIIa). Overall, the MKM results summarized in **Table 1**, **Table 2**, and **Figure 3(d)** show that fractional CO and O_2 order come from multiple competing rate-determining processes. Our computational results suggest that there is an ensemble of active surface species and pathways persisting on the catalyst during reaction.

Table 2: Computed degree of rate control (DRC) obtained from the microkinetic modeling (MKM) at reaction conditions (T = 160 °C, P_{CO} = 1 kPa, P_{O2} = 10 kPa, conversion = 5%) for the TOF-determining transition states (TDTS)

Label	Reaction	Type of reaction	DRC
R5	$Pt(CO)(O_2)[V] \rightarrow TS\ I \rightarrow\ Pt(CO)(O)(O)[VI]$	Surface, O_2 dissociation	0.45
R9	$Pt(O)(CO)(O_2)[Xa] + CO_{gas} \rightarrow\ TS\ IIIa \rightarrow\ Pt(CO)(CO_2)(O_2)\ [XIa]$	Eley-Rideal, CO_2 formation	0.24
R6	$Pt(CO)(O)(O)[VI] \rightarrow TS\ IIa \rightarrow\ Pt(O)(CO_2)[VIIa]$	Surface, CO_2 formation	0.18
R8	$Pt(O)(CO)[IX] + O_{2_{gas}} \rightarrow Pt(O)(CO)(O_2)\ [Xa]$	Adsorption	0.05

Origin of Partial Orders and Apparent Activation Energy

The main TDTS of the complete reaction network (TS I) and the main TDI (IV and V) are located along the black pathway, associated with the re-oxidation of the catalyst. Following the approach proposed by Campbell and coworkers [43–45], the resulting reaction order depends on the choice of the TDI species: If structure IV is selected, one O_2 adsorption step occurs between TDI and TDTS so that the O_2 order is 1; If structure V is selected, O_2 is already adsorbed, hence the order is zero. Since both IV and V have TDI nature, the overall order is a weighted average, hence close to 0.5. No CO adsorption occurs between TDI and TDTS along this pathway, so that the CO order should be zero. This is confirmed by a model MKM simulation where only the black pathway of **Figure 2** is included (see **Figure 4** (c) and

Table 3) where the O_2 order is mainly unchanged while the CO order drops to 0.03.

Table 3: Results from the decomposed microkinetic analysis of the three simpler reactive cycles within the complete reaction cycle

	All combined	Black	Black + Blue	Black + Red
TOF (s^{-1})	3.3 x 10^3	5. 3 x 10^3	4.2 x 10^3	2.1 x 10^3
CO order	0.24	0.03	0.33	0.01
O_2 order	0.46	0.53	0.38	0.2
E_{app} (eV)	0.47	0.38	0.29	1.15

The origin of the partial CO order is located in the blue pathway. Structure XIa along this path has a significant coverage (~0.17) and hence some TDI nature, associated with TS IIIa as a TDTS (DRC 0.24). This Eley-Rideal CO oxidation step obviously sees a CO adsorption between the TDI and the TS, so that the CO order is 1, but no O_2 adsorption so that the O_2 order is zero. The combined orders when mixing the blue pathway with the black pathway depend on the weight of the pathways in the rate. A model MKM simulation including only the black and blue paths gives 0.33 and 0.38 for the CO and O_2 order, respectively, in good agreement with our qualitative discussion above.

The involvement of a 2nd CO from the gas-phase (during the ER steps) has been confirmed by multiple *in situ* DRIFTS experiments. The CO adsorption peak after cooling down (under CO and O_2 flow) from steady-state CO oxidation (at 160 °C) to 35 °C and -75 °C shows identical shape and intensity (**Figure S11**). This shows that there are no bare Pt sites (without chemisorbed CO) during steady-state CO oxidation, indicating that the positive CO order is not due to weak CO adsorption on bare Pt sites, but rather due to a 2nd CO from the gas phase reacting with adsorbed oxygen. To investigate further, we performed $^{13}CO/^{12}CO$ exchange experiments at 160 °C both in the presence and absence of O_2, *i.e.* ^{13}CO oxidation and ^{13}CO pulse (**Figure S12 (a) and (b),** respectively). Exchange of ^{13}CO with ^{12}CO occurs during CO oxidation, as evident from the evolution of the peak centered at ~2066 cm^{-1}, but with an exchange rate (~36% in 30 mins) that is slower than the turnover number in the equivalent time (~5 turnovers in 30 mins) suggesting a 2nd CO is likely involved but that this is not the only CO oxidation pathway. If the chemisorbed CO

was the only one involved in the reaction, all ^{12}CO would have been replaced by ^{13}CO in 30 mins because of the 5 turnovers observed. The partial exchange between ^{12}CO and ^{13}CO can be explained further by considering the black and red pathways presented in the reaction mechanism scheme in **Figure 2** (a). If the reaction proceeds via the black pathway, the chemisorbed CO turns over and $^{12}CO/^{13}CO$ exchange becomes possible, whereas, in the red pathway, the chemisorbed CO stays unreacted resulting in no $^{12}CO/^{13}CO$ exchange. Both "Black" and "Red" pathways being present in a competitive fashion, therefore, leads to partial exchange between ^{12}CO and ^{13}CO. Interestingly, the absence of gas-phase O_2 seems to promote the exchange of ^{13}CO with ^{12}CO, which was also observed for Ir_1/TiO_2[31]. The experimental results therefore confirm the simultaneous presence of ER and LH CO oxidation steps in the mechanism as proposed by our calculations (black and blue paths).

The red pathway introduces the TDI structure VIIIb ($Pt(CO_3)(CO)$ with overall coverage 0.2) and explains the carbonate formation leading to partial poisoning of the active site. A model simulation including only the black and red paths (**Figure 4** (c)) provides a higher carbonate coverage (0.6) compared to its overall coverage. This is due to the fact that in the overall system, the blue pathway opens up an extra channel to consume structure IX and hence the carbonate structure VIIIb (**Figure 2**).

If we now focus on the apparent activation energy, it also has a composite nature. Since the activation energy is an enthalpy, it should be obtained from the enthalpy differences for the TOF-determining processes (see **Figure S15** in SI). Contributions from the initial O_2 dissociation pathway (black path) are –0.25 eV for IV-TSI and +0.76 eV for V-TSI, while from the red path, the carbonate decomposition corresponds to an enthalpy of +1.5 eV (CO_2 release), and from the blue path, Xa-TSIIIa is associated to a barrier of 0.33 eV. The overall computed value is 0.47 eV, corresponding to a rate-weighted combination of the various active pathways, while model simulations with only part of the paths can provide strongly altered values (**Table 3**). For example, only "black + red" path shows an effective barrier of 1.15 eV, while the "black + blue" path shows an effective barrier of 0.29 eV.The overall kinetics and kinetic parameters therefore result from the combination of different reaction branches in the mechanism. Small energy differences in the profile can change the contribution of each path in the reaction rate and affect the orders and apparent activation energy. Computational results can be sensitive to errors in free energy values from various approximations (DFT energy, entropy values), meaning it is very challenging to obtain accurate values [34]. The impact of the sensitivity of the DFT accuracy is further illustrated in the supporting information (**Figure S14** and associated discussion in SI), where changes by 0.2

eV (which is within the approximate error of DFT)[46] in the transition state energies could lead to TOF value of 24 s^{-1}- a value two orders of magnitude lower compared to the TOF obtained from the unmodified Gibbs free energies. This is a phenomenon previously seen in the literature involving MKM, where finding the accurate and reliable absolute value of TOF solely from quantum chemical modeling is not always a straightforward path. A work by Guo et al. confirms the potential discrepancy in the TOF with variability between 10^{-1} to 10^{5} s^{-1} in magnitude, and further suggests that addressing the over-binding behavior of DFT would lead to better agreement with the experiment[47]. Few solutions to overcome this issue have been proposed in the literature, such as recalculation for more accurate O_2 binding and dissociation energies[48] , or simply acknowledging this discrepancy with sensitivity analysis[49]. Nevertheless, the destabilization of TSs did not impact the partial order behavior of CO and O_2. Recent works suggest modification of the Gibbs free energy profile can improve the MKM accuracy, parameterized against experimental observation[50,51]. Further modifications on the free energy profile within the limits of DFT accuracy are then incorporated in the current study to see whether MKM can match the experimental findings, where CO order is larger than that of O_2. From our previous analyses of decoupled MKM for the different cycles, it is clear that the CO order stems from the blue pathway, thus to encourage larger partial order of CO, the energies of the intermediates in the blue pathway are lowered by 0.125 eV, still within the error of DFT. This modification indeed results in the CO order being slightly larger than O_2 order (0.27 and 0.24, respectively). A final effort to lower the TOF is performed by stabilizing intermediates IV and V by 0.08 eV, which yields a final TOF of 2.1 s^{-1} and an apparent activation energy of 0.84 eV, much closer to the observed experimental values. Our limited sensitivity analysis approach shows that small energy changes, well within the error of DFT, can have significant consequences on calculated kinetic parameters. Combining theory and experiment is hence essential to provide detailed insights in such cases where reaction channels/branches compete.

Conclusions

In this study, we investigated the mechanism of CO oxidation on a single-atom Pt supported on anatase TiO_2 (Pt_{SA}/a-TiO_2) using a combination of DFT calculations, microkinetic analysis, experimental kinetic measurements, and several *in situ/operando* spectroscopic techniques. Despite remaining as isolated atoms, Pt_{SA} species shows dynamic coordination behavior under different gas environments, *i.e.*, oxidative, reductive, and reactive conditions. We show that despite the apparently simple system of a supported single Pt atom, the CO oxidation reaction on Pt_{SA}/a-TiO_2 (101) involves a complex reaction mechanism consisting of initiation steps followed

by a reactive cycle involving multiple competing pathways. As shown by the combination of DFT calculations and DRIFTS experiments, under reducing conditions the initial catalyst consists of a Pt_{SA} structure having an adsorbed/supported Pt atom on the anatase-TiO_2 (101) with one oxygen vacancy. The initiation steps consist of CO adsorption and healing of O vacancy with an O_2 molecule, followed by an Eley-Rideal type CO oxidation on the surface O_2 species involving another gas-phase CO and forming the supported Pt(CO) structure. The subsequent reactive cycle starts from the oxidation of Pt(CO) with O_2, and proceeds via competitive CO oxidation events occurring either from chemisorbed CO (Langmuir-Hinshelwood mechanism) or form additional gas-phase CO (Eley-Rideal mechanism) forming a Pt(O)(CO) species. Another CO oxidation step follows, also through competition between two mechanisms, completing the cycle to form the initial Pt(CO) species. Microkinetic modeling reveals that the most abundant intermediates during steady-state CO oxidation are Pt(CO) and $Pt(O_2)CO$, both exhibiting CO stretching frequencies close to the experimentally observed value of 2115 cm^{-1}. The kinetic measurements and the microkinetic modeling simulations from first principles show fractional positive CO and O_2 orders, originating from an O_2 dissociation and an Eley-Rideal CO_2 formation steps exhibiting the highest degree of rate control. Our study also shows that the reaction pathways proceed with the involvement of oxygen adatoms directly provided by O_2 dissociation, and not lattice oxygens as it would be the case for a Mars-van Krevelen mechanism. Our results show that microkinetic modeling is sensitive to the uncertainties in energies and barriers from DFT, and without experiments, could lead to incorrect conclusions regarding reaction rate, dominant reaction pathway, and most abundant reaction intermediates. Overall, our findings shed light on the intricate reaction pathways followed by even a seemingly simple single-atom catalyst system for a model CO oxidation reaction.

Computational Methods

Anatase TiO_2(101) was chosen as the support because it is the most stable facet, followed by the (010) and the (001) facets with surface energies of 0.44, 0.53 and 0.9 $J.m^{-2}$, respectively, with the (101) facet dominating (>94%) the surface of nanoparticles [52,53]. The Vienna Ab Initio Simulation Package was used for the density functional theory computations (VASP) [54,55]. All calculations were performed using the Perdew-Burke-Ernzerhof (PBE) functional to describe the exchange and correlation energy [56]. In order to correctly include the van der Waals interactions, the dDsC dispersion correction was added [57,58]. The electron-ion interactions were described by the Projector Augmented Wave (PAW) approach. One-electron functions were developed on a plane wave basis set and a 500 eV cutoff was chosen [55,59,60]. Following the Dudarev approach, Ti was

given an effective Hubbard U (DFT+U) parameter of 4.2 eV due to the onsite coulomb repulsion of the Ti 3d orbitals [61,62]. The value of 4.2 eV was chosen because it accurately captures the characteristics of the electronic structure that were seen with anatase TiO_2 in experimental settings, particularly the localized nature of electrons on surfaces with oxygen vacancies [63]. The electronic energies were converged within a 10^{-6} eV accuracy and atomic force convergence criterion was set to 0.03 eV/atom. The transition states structures and energies were calculated using the Nudged Elastic Band Method including 8 images.

The periodic slab of anatase TiO_2 (101) was cut from a TiO_2 bulk of lattice constant: a = 3.83 Å and c = 9.63 Å. The slab contains 4 O-Ti-O layers with the first tri-layer constrained to simulate the bulk during geometric relaxation. Vacuum length of 17 Å was incorporated in the z-direction to avoid interactions between periodic images. The *ab initio* thermodynamics analysis to study the stability of Pt_{SA}/a-TiO_2(101) was performed using the following reaction balance:

$$TiO_{2\,(pris)} + Pt_{(bulk)} + \frac{x}{2} O_{2_{(g)}} \rightarrow TiO_2Pt_1.xO_{ad} + y\, Ti_{substituted} \quad (1)$$

Where x (x=0-2) describes the total surface O adatom and y (y=0-1) describes if Pt is substituting Ti. We assume that the chemical potential of substituted Ti is in equilibrium with the bulk TiO_2, and that the Pt_{SA} is in equilibrium with bulk Pt (bulk Pt_4 is chosen due to arbitrary modeling convenience and does not have any difference with bulk model containing 1 Pt). This reaction balance thus results in the following equation:

$$G = E_{TiO_2Pt_1.xO_{ad}} + y\left(E_{TiO_{2\,bulk}} - 2\mu_O\right) - E_{TiO_2(pris)} - E_{Pt_{(bulk)}} - x\,\mu_O \quad (2)$$

E denotes the electronic energy obtained from DFT calculation and μ_O describe the oxygen chemical potential at various temperature and pressure. To account for the anharmonicity of the vibrational spectra simulation, the values obtained by the simulation are usually normalized with respect to a reference, where CO gas is the common choice. However, CO gas is not an appropriate structure to obtain a scaling factor for Pt(+2) species as it fails to reproduce the CO stretches of Pt(II)-CO complexes ($PtCl_2(CO)_2$). [64] Hence, in this work, the CO stretch is normalized by $PtCl_2(CO)_2$ instead of gas phase CO to account for this error. The Pt, O adatoms and surface O_{2c} interacting with the isolated Pt are included in the dynamic space for all vibrational analysis calculations.

Experimental Methods

Catalyst Synthesis and Pretreatment

The single-atom Pt/a-TiO_2 catalyst used in this study was synthesized by wet impregnation (WI) method with nominal Pt loading (w/w) of 0.025%. A pH of ~13.7 was used for the synthesis considering the point of zero charge (PZC) of anatase TiO_2 is ~6.4 (**Figure S1**). Tetraammineplatinum (II) nitrate ($[Pt(NH_3)_4](NO_3)_2$) was used as the Pt precursor. Anatase TiO_2 was used as support and was purchased from the U.S. Research Nanomaterials (99.5%, stock #US3838) with an average crystallite size of ~9 nm and specific surface area of 197 m^2/g (**Figure S2**). The crystallite size was estimated using the Scherrer equation and the line broadening of anatase TiO_2 diffraction peaks from XRD analysis (**Figure S3** and **Table S1**). Specific surface area was obtained from BET surface area analysis (**Figure S2**) using 3Flex from Micromeritics Instrument Corporation. First, fresh anatase TiO_2 support was sieved to powder finer than 75 µm and dried in a vacuum oven at 120 °C overnight before use. Pt/a-TiO_2 sample with 0.025% Pt loading was prepared in 1 g batch. An appropriate amount (based on the nominal Pt loading) of the sieved and dried anatase TiO_2 support was weighed and dispersed in ammonium hydroxide solution (NH_4OH with pH of ~13.7; ACS reagent, 29.8% NH_3 basis, Sigma-Aldrich 221228, lot #SHBJ4683) in a glass bottle by stirring at 700 rpm on a stirrer hotplate at room temperature. The dispersion volume was 450 mL which resulted in a surface loading of 644 m^2/L (calculated using the following equation).

$$Surface\ loading = \frac{mass\ of\ the\ supprot \times surface\ area\ of\ the\ support}{volume\ of\ the\ support\ dispersion} \quad (3)$$

An appropriate amount (based on the nominal Pt loading) of tetraammineplatinum(II) nitrate precursor ($[Pt(NH_3)_4](NO_3)_2$; 50.3% Pt basis, Aldrich 278726, lot #MKBN9761V) was weighed and dissolved in ~30 mL of the same ammonium hydroxide solution used for support dispersion. The Pt precursor solution was then slowly added into the support dispersion, while constantly being stirred at 700 rpm, using a syringe pump at a rate of 2 ml/hr. Following the deposition of Pt, the catalyst solution was left on the hotplate overnight at 50 °C to evaporate the solvent. The catalyst samples were then dried in a muffle furnace at 120 °C (ramp rate of 1 °C/min) for 12 hr and calcined at 450 °C (ramp rate of 5 °C/min) for 4 hr. The calcination temperature was limited to 450 °C to maintain the anatase phase which has been reported to be transformed to rutile at ~500 °C [65,66].

Moreover, this temperature was reported to be sufficient to completely remove the amine and nitrate ligands from the tetraammineplatinum(II) nitrate precursor [67]. The calcined sample was pretreated *in situ* prior to any tests described in the subsequent sections. The *in situ* pretreatment procedure consisted of the following steps: oxidation under 10 kPa O_2 flow (balance N_2 to

atmospheric pressure at a total flow rate of 100 sccm; O_2 = 10 sccm and N_2 = 90 sccm) at 300 °C for 1 hr followed by reduction under 20 kPa H_2 flow (balance N_2 to atmospheric pressure at a total flow rate of 100 sccm; H_2 = 20 sccm and N_2 = 80 sccm) at 350 °C for 2 hr. The reduction temperature was determined to be 350 °C based on H_2-TPR experiments for similar Pt/a-TiO_2 samples reported previously [68]. H_2 was purified with high-capacity moisture and oxygen traps, and O_2 was purified with high-capacity moisture traps from Restek Corporation. To confirm the phase and determine the crystallite size, we performed X-ray diffraction (XRD) on the calcined (at 450 °C for 4 hr) anatase TiO_2 and the 0.025% Pt/a-TiO_2 catalyst sample after CO oxidation reaction (denoted as "spent catalyst" in the figure). The XRD patterns (shown in **Figure S3**) show that TiO_2 remains as anatase phase after calcination for both pure TiO_2 and Pt_{SA}/TiO_2 sample. Specific surface area for calcined anatase TiO_2 and spent Pt_{SA}/a-TiO_2 (after CO oxidation) were found to be 81 and 70 m^2/g, with average crystallite size of anatase TiO_2 being 17.8 nm and 20.5 nm, respectively (presented in **Figure S2** and **Table S1**).

Aberration-Corrected High-Angle Annular Dark-Field Scanning Transmission Electron Microscopy

Aberration-corrected scanning transmission electron microscopy (AC-STEM) images of the 0.025% Pt/a-TiO_2 (Pt_{SA}/a-TiO_2) catalyst were taken *ex situ* after CO oxidation kinetics experiment. Reduction pretreatment was performed according to the procedure detailed in the previous section and CO oxidation was performed under 1 kPa CO and 10 kPa O_2 (balance N_2 at atmospheric pressure with a total gas flow rate of 75 sccm) at 160 °C for extended period (~3 hours) following the *in situ* reduction pretreatment. The images were taken on a JEOL JEM-ARM200F atomic resolution electron microscope at an acceleration voltage of 200 kV equipped with EDS detector EX-24221M1G5T.

Diffuse-Reflectance Infrared Fourier Transform Spectroscopy (DRIFTS)

In situ/*operando* diffuse reflectance infrared Fourier transform spectroscopy (DRIFTS) of CO adsorption was performed under ambient pressure to investigate adsorption and reactivity of CO at different states of the Pt_{SA}/a-TiO_2 catalysts. The DRIFTS experiments were performed on a Thermo Scientific Nicolet iS-50R FTIR Spectrometer equipped with a liquid nitrogen-cooled mercury-cadmium-telluride infrared detector (MCT-A). Approximately 50 mg of the catalyst sample was loaded into the sample cup, equipped with a K-type thermocouple for temperature monitoring, of an in situ Praying Mantis diffuse reflection cell (Harrick Scientific Products). The DRIFTS cell/chamber was sealed and connected to a flow system

with temperature control, and gases were flowed through the sample at atmospheric pressure. The spectra, reported in Kubelka-Munk (KM) units, were collected with a spectral resolution of 4 cm^{-1} and a data spacing of 0.482 cm^{-1}, and each was an average of 32 scans. Before collecting the spectra, the catalysts were prepared by the *in situ* reduction pretreatment as delineated in the "Catalyst Synthesis and Pretreatment" section. After *in situ* pretreatment, a background spectrum was collected under N_2 flow at room temperature, which was then subtracted from the series of subsequent spectra (for all types of experiments we performed: CO adsorption after reduction pretreatment, CO oxidation after reduction pretreatment, and CO adsorption, isotopic exchange experiments, etc.; the details are given below). The CO (5%, balance N_2) and O_2 (100%, UHP) were obtained from Airgas Inc., whereas N_2 was obtained from in-house liquid N_2 boil-off. N_2 was purified with high-capacity moisture and oxygen traps from Restek Corporation. CO was purified with a metal carbonyl purifier (Metal-X Purification Medium, NANOCHEM Corrosive Gas Purifiers, Matheson Tri-Gas, Inc.) to remove trace amount of metal carbonyl and a molecular sieve 3 Å (8-12 mesh) trap to remove trace (ppm) levels of CO_2. All feed gas flows were controlled by mass flow controllers (5850EM) from Brooks Instrument.

CO adsorption experiments were performed with 0.5 kPa CO flow (balance N_2 to atmospheric pressure with a total gas flow rate of 100 sccm) at 35 °C. CO oxidation was performed under 1 kPa CO and 10 kPa O_2 (balance N_2 to atmospheric pressure with a total gas flow rate of 75 sccm) at 160 °C for 20 mins following the *in situ* oxidation and reduction pretreatment. First, *1 kPa CO was flowed at 35 °C and after 2-3 mins, 10 kPa O_2 was added (balance N_2 to atmospheric pressure at a total flow rate of 75 sccm; CO = 15 sccm, O_2 = 7.5 sccm and N_2 = 52.5 sccm). The CO and O_2 co-flow at 35 °C was maintained for ~5 mins before ramping up to 160 °C at 10 °C/min. For isotopic ^{18}O-^{16}O switching experiment, the sample was heated under CO and $^{16}O_2$ flow to 160 °C and allowed to react for 30 mins to reach steady-state. After that, $^{16}O_2$ was abruptly switched with $^{18}O_2$ using a 4-position 4-port manual switching valve (IDEX Health & Science LLC; Mfr #V-101T) and the reaction under 1 kPa CO and 10 kPa $^{18}O_2$ was run for 15 mins to reach stable state. $C^{16}O_2$ (m/z = 44) and $C^{16}O^{18}O$ (m/z = 46) signals were recorded in a mass spectrometer and compared during these procedures. Signals for $^{16}O_2$ (m/z = 32), $^{18}O_2$ (m/z = 36), and CO (m/z = 12) were also recorded.*

In situ/operando DRIFTS was also utilized to perform temperature-programmed desorption (TPD) of the CO chemisorbed during steady-state CO oxidation to estimate its binding energy. First, CO oxidation was performed on the reduced catalyst at 160 °C with 1 kPa CO, 10 kPa O_2, and balance

N_2 at 75 sccm total gas flow for ~20 mins after the CO adsorption DRIFTS spectrum reached steady-state condition. Afterwards, the sample was cooled down to 35 °C under the same gas composition. For TPD, CO and O_2 flow were then stopped while the remaining CO and O_2 in the DRIFTS chamber were flushed with N_2 flow. The sample was then heated to ~300 °C at different heating rates (5K/min, 10K/min, and 15K/min in three different experiments) under only N_2 flow, while DRIFTS spectra were being recorded simultaneously.

X-ray absorption Spectroscopy (XAS)

The 0.025% Pt/a-TiO_2 catalyst was also characterized by *in situ* X-ray absorption spectroscopy (XAS) at the Pt L_3-edge (11564 eV). The sample was oxidized and reduced as mentioned previously and then exposed to CO oxidation (1% CO and 10% O_2 with balance He) at 160 °C for one hour and then measured after cooling down to 35 °C in CO and O_2 flow. The measurements were performed at National Synchrotron Light Source II (NSLS-II) Inner Shell Spectroscopy (ISS) at beamline 08-ID (BL 08-ID[1]). The beamline has a damping wiggler source with a beam size of 1 mm × 1 mm and a flux density of 4×10^{12} photons.s^{-1}.mm^{-2}. Around 100 mg of catalyst sample was loaded into a custom-built 4 mm ID quartz tube. A reactor custom-built at NSLSII was used for the experiments with the temperature measured via a thermocouple inserted through the reactor tube immediately downstream of the catalyst, only being separated by a thin layer of quartz wool. The gas flows were controlled by mass flow controllers (MFCs) and continuously monitored by a mass spectrometer. The X-ray absorption fine structure (XAFS; consisting of both x-ray absorption near-edge spectroscopy, XANES, and extended x-ray absorption fine-structure spectroscopy, EXAFS) scans were collected in total fluorescence mode while the sample was under He flow after CO oxidation reaction.

CO Oxidation Kinetic Measurements

To gain insight into activity and reaction mechanism, we performed CO oxidation kinetic measurements under differential conditions (kinetic regime, *i.e.*, very low conversion of ≤ 5% in the absence of mass and heat transport limitations) in a quartz tube packed-bed reactor system (7 mm ID). We used the calcined 0.025% Pt/a-TiO_2 catalyst with powder size ranging between 106-300 µm without any dilution since dilution studies showed no effect on the measured intrinsic rate. Dilution studies were performed following the Koros-Nowak test[69] and it was determined that no dilution was needed due to the low weight loading, 0.025% Pt. Around 500 mg of the calcined 0.025% Pt/TiO_2 sample (bed length 6-7 cm) was loaded in the quartz reactor tube and the sample went through *in situ* oxidation and reduction steps (as described above) prior to the kinetic

measurements. The pressure drop across the catalyst bed was negligible. A K-type thermocouple (Omega Engineering, Inc.) attached at the center of the catalyst bed on the outside of the tube for temperature monitoring. A split furnace utilizing clamshell heating elements (from The Mellen Company, Inc.) equipped with a Watlow temperature controller was used for heating purposes. After pretreatment, the samples were cooled down to 35 °C under inert flow only. CO was then mixed with O_2 and He at 35 °C to achieve 1 kPa CO, 10 kPa O_2, and balance He to atmospheric pressure at 75 sccm total flow rate. The reactor was then heated to 160 °C at 5 °C/min ramp rate and 20 mins was allowed under reaction gas composition at 160 °C to stabilize. To measure the effect of temperature on reaction rate and extract the apparent activation energy (E_{app}), Arrhenius experiment was performed between 150 and 170 °C with 1 kPa CO, 10 kPa O_2, and balance He to atmospheric pressure at 75 sccm total flow rate. To measure the effect of CO and O_2 partial pressure on TOF at 160 °C, 0.4-1 kPa CO and 10 kPa O_2 was used for the effect of CO partial pressure and 1 kPa CO and 4-12 kPa O_2 was used for the effect of O_2 partial pressure with balance He to atmospheric pressure at 75 sccm total flow rate for both cases. No evidence of agglomeration of the Pt single atoms was observed under the conditions used in this study. However, some agglomeration was observed starting at a temperature of ~200 °C and higher. The catalyst was stable during catalytic measurements and the activity dropped by ~20% after ~18 hr time on stream. Under all gas flow and temperature conditions, CO conversion was at or below 5%. The outlet gas composition was measured by a gas chromatograph, Micro GC Fusion Gas Analyzer from Inficon Inc. with two modules, each with a separate carrier gas, injector, column, and thermal conductivity detector (TCD). Column A (Rt-Molsieve 5a, 0.25 mm ID (10 m)) uses Ar as the carrier gas and Column B (Rt-Q-Bond, 0.25 mm ID (12 m) uses He as the carrier gas. The purification process and composition of all the individual feed gases are the same as described in previous sections. The reaction rates were normalized by the moles of surface Pt which was equal to the moles of total Pt considering the singly-dispersed Pt atoms.

Supporting Information

Additional characterization and results, such as BET, powder XRD, STEM, DRIFT, $^{12}CO/^{13}CO$ exchange experiment and $^{18}O_2$ labelling experiment. Details of computational methods and results, as structure of intermediates and microkinetic modeling methodology.

Acknowledgements

CT and PS acknowledge support from the U.S. Army under Program No. W911NF-21-1-0361. MY and AMK acknowledge support from the U.S. Army Research Laboratory and the U.S. Army

Research Office under Grant No. W911NF-20-2-0058. The views and conclusions contained in this document are those of the authors and should not be interpreted as representing the official policies, either expressed or implied, of the Army Research Office or the U.S. Government. The U.S. Government is authorized to reproduce and distribute reprints for Government purposes notwithstanding any copyright notation herein. This research used 8-ID (ISS) beamline of the National Synchrotron Light Source II, a U.S. Department of Energy (DOE) Office of Science User Facility operated for the DOE Office of Science by Brookhaven National Laboratory under Contract No. DE-SC0012704. STEM imaging was performed through support by the Cooperative Research Program of Institute for Catalysis, Hokkaido University (20A1004 and 22DS0123). This work used computational and storage services associated with the Hoffman2 Shared Cluster provided by UCLA Office of Advanced Research Computing's Research Technology Group and by the hardware at Virginia Tech's Advanced Research Computing. This work used Bridges-2 at Pittsburgh Supercomputing Center through allocation CHE170060 from the Advanced Cyberinfrastructure Coordination Ecosystem: Services & Support (ACCESS) program, which is supported by National Science Foundation grants #2138259, #2138286, #2138307, #2137603, and #2138296.

References

(1) De, S.; Burange, A. S.; Luque, R. Conversion of Biomass-Derived Feedstocks into Value-Added Chemicals over Single-Atom Catalysts. *Green Chemistry* **2022**, *24* (6), 2267–2286. https://doi.org/10.1039/D1GC04285H.

(2) Shan, J.; Li, M.; Allard, L. F.; Lee, S.; Flytzani-Stephanopoulos, M. Mild Oxidation of Methane to Methanol or Acetic Acid on Supported Isolated Rhodium Catalysts. *Nature* **2017**, *551* (7682), 605–608. https://doi.org/10.1038/nature24640.

(3) Lin, L.; Yao, S.; Gao, R.; Liang, X.; Yu, Q.; Deng, Y.; Liu, J.; Peng, M.; Jiang, Z.; Li, S.; Li, Y.-W.; Wen, X.-D.; Zhou, W.; Ma, D. A Highly CO-Tolerant Atomically Dispersed Pt Catalyst for Chemoselective Hydrogenation. *Nat Nanotechnol* **2019**, *14* (4), 354–361. https://doi.org/10.1038/s41565-019-0366-5.

(4) Yan, H.; Cheng, H.; Yi, H.; Lin, Y.; Yao, T.; Wang, C.; Li, J.; Wei, S.; Lu, J. Single-Atom Pd $_1$ /Graphene Catalyst Achieved by Atomic Layer Deposition: Remarkable Performance in Selective Hydrogenation of 1,3-Butadiene. *J Am Chem Soc* **2015**, *137* (33), 10484–10487. https://doi.org/10.1021/jacs.5b06485.

(5) Yan, X.; Duan, P.; Zhang, F.; Li, H.; Zhang, H.; Zhao, M.; Zhang, X.; Xu, B.; Pennycook, S. J.; Guo, J. Stable Single-Atom Platinum Catalyst Trapped in Carbon Onion Graphitic Shells for Improved Chemoselective Hydrogenation of Nitroarenes. *Carbon N Y* **2019**, *143*, 378–384. https://doi.org/10.1016/j.carbon.2018.11.021.

(6) Zhang, L.; Zhou, M.; Wang, A.; Zhang, T. Selective Hydrogenation over Supported Metal Catalysts: From Nanoparticles to Single Atoms. *Chem Rev* **2020**, *120* (2), 683–733. https://doi.org/10.1021/acs.chemrev.9b00230.

(7) Qiao, B.; Wang, A.; Yang, X.; Allard, L. F.; Jiang, Z.; Cui, Y.; Liu, J.; Li, J.; Zhang, T. Single-Atom Catalysis of CO Oxidation Using Pt1/FeOx. *Nat Chem* **2011**. https://doi.org/10.1038/nchem.1095.

(8) Ding, K.; Gulec, A.; Johnson, A. M.; Schweitzer, N. M.; Stucky, G. D.; Marks, L. D.; Stair, P. C. Identification of Active Sites in CO Oxidation and Water-Gas Shift over Supported Pt Catalysts. *Science (1979)* **2015**, *350* (6257), 189–192. https://doi.org/10.1126/science.aac6368.

(9) Therrien, A. J.; Hensley, A. J. R.; Marcinkowski, M. D.; Zhang, R.; Lucci, F. R.; Coughlin, B.; Schilling, A. C.; McEwen, J.-S.; Sykes, E. C. H. An Atomic-Scale View of Single-Site Pt Catalysis for Low-Temperature CO Oxidation. *Nat Catal* **2018**, *1* (3), 192–198. https://doi.org/10.1038/s41929-018-0028-2.

(10) Zhang, Z.; Zhu, Y.; Asakura, H.; Zhang, B.; Zhang, J.; Zhou, M.; Han, Y.; Tanaka, T.; Wang, A.; Zhang, T.; Yan, N. Thermally Stable Single Atom Pt/m-Al2O3 for Selective Hydrogenation and CO Oxidation. *Nat Commun* **2017**, *8*. https://doi.org/10.1038/ncomms16100.

(11) Ji, S.; Chen, Y.; Wang, X.; Zhang, Z.; Wang, D.; Li, Y. Chemical Synthesis of Single Atomic Site Catalysts. *Chem Rev* **2020**, *120* (21), 11900–11955. https://doi.org/10.1021/acs.chemrev.9b00818.

(12) Lu, Y.; Zhou, S.; Kuo, C.-T.; Kunwar, D.; Thompson, C.; Hoffman, A. S.; Boubnov, A.; Lin, S.; Datye, A. K.; Guo, H.; Karim, A. M. Unraveling the Intermediate Reaction Complexes and Critical Role of Support-Derived Oxygen Atoms in CO Oxidation on Single-Atom Pt/CeO2. *ACS Catal* **2021**, *11* (14), 8701–8715. https://doi.org/10.1021/acscatal.1c01900.

(13) Kottwitz, M.; Li, Y.; Palomino, R. M.; Liu, Z.; Wang, G.; Wu, Q.; Huang, J.; Timoshenko, J.; Senanayake, S. D.; Balasubramanian, M.; Lu, D.; Nuzzo, R. G.; Frenkel, A. I. Local Structure and Electronic State of Atomically Dispersed Pt Supported on Nanosized CeO_2. *ACS Catal* **2019**, *9* (9), 8738–8748. https://doi.org/10.1021/acscatal.9b02083.

(14) DeRita, L.; Resasco, J.; Dai, S.; Boubnov, A.; Thang, H. V.; Hoffman, A. S.; Ro, I.; Graham, G. W.; Bare, S. R.; Pacchioni, G.; Pan, X.; Christopher, P. Structural Evolution of Atomically Dispersed Pt Catalysts Dictates Reactivity. *Nat Mater* **2019**. https://doi.org/10.1038/s41563-019-0349-9.

(15) Dessal, C.; Len, T.; Morfin, F.; Rousset, J. L.; Aouine, M.; Afanasiev, P.; Piccolo, L. Dynamics of Single Pt Atoms on Alumina during CO Oxidation Monitored by Operando X-Ray and Infrared Spectroscopies. *ACS Catal* **2019**, *9* (6), 5752–5759. https://doi.org/10.1021/acscatal.9b00903.

(16) Moses-Debusk, M.; Yoon, M.; Allard, L. F.; Mullins, D. R.; Wu, Z.; Yang, X.; Veith, G.; Stocks, G. M.; Narula, C. K. CO Oxidation on Supported Single Pt Atoms: Experimental and Ab Initio Density Functional Studies of CO Interaction with Pt Atom on θ-Al 2O3(010) Surface. *J Am Chem Soc* **2013**, *135* (34), 12634–12645. https://doi.org/10.1021/ja401847c.

(17) Diasanayake, M. A. K. L.; Senadeera, G. K. R.; Sarangika, H. N. M.; Ekanayake, P. M. P. C.; Thotawattage, C. A.; Divarathne, H. K. D. W. M. N. R.; Kumari, J. M. K. W. TiO2 as a Low Cost, Multi Functional Material. *Mater Today Proc* **2016**, *3*, S40–S47. https://doi.org/10.1016/j.matpr.2016.01.006.

(18) Cargnello, M.; Gordon, T. R.; Murray, C. B. Solution-Phase Synthesis of Titanium Dioxide Nanoparticles and Nanocrystals. *Chem Rev* **2014**, *114* (19), 9319–9345. https://doi.org/10.1021/cr500170p.

(19) Banfield, J. Thermodynamic Analysis of Phase Stability of Nanocrystalline Titania. *J Mater Chem* **1998**, *8* (9), 2073–2076.

(20) Hanaor, D. A. H.; Sorrell, C. C. Review of the Anatase to Rutile Phase Transformation. *J Mater Sci* **2011**, *46* (4), 855–874.

(21) Periyat, P.; Naufal, B.; Ullattil, S. G. A Review on High Temperature Stable Anatase TiO2 Photocatalysts. In *Materials Science Forum*; Trans Tech Publ, 2016; Vol. 855, pp 78–93.

(22) Tanemura, S.; Miao, L.; Wunderlich, W.; Tanemura, M.; Mori, Y.; Toh, S.; Kaneko, K. Fabrication and Characterization of Anatase/Rutile–TiO2 Thin Films by Magnetron Sputtering: A Review. *Sci Technol Adv Mater* **2005**, *6* (1), 11–17.

(23) Monai, M.; Montini, T.; Fornasiero, P. Brookite: Nothing New under the Sun? *Catalysts* **2017**, *7* (10), 304.

(24) Wang, C.; Deng, Z.-X.; Li, Y. The Synthesis of Nanocrystalline Anatase and Rutile Titania in Mixed Organic Media. *Inorg Chem* **2001**, *40* (20), 5210–5214. https://doi.org/10.1021/ic0101679.

(25) Chen, L.; Unocic, R. R.; Hoffman, A. S.; Hong, J.; Braga, A. H.; Bao, Z.; Bare, S. R.; Szanyi, J. Unlocking the Catalytic Potential of TiO_2 -Supported Pt Single Atoms for the Reverse Water–Gas Shift Reaction by Altering Their Chemical Environment. *JACS Au* **2021**, *1* (7), 977–986. https://doi.org/10.1021/jacsau.1c00111.

(26) Thang, H. V.; Thang, H. V.; Pacchioni, G.; DeRita, L.; Christopher, P. Nature of Stable Single Atom Pt Catalysts Dispersed on Anatase TiO2. *J Catal* **2018**, *v. 367*, 104-114–2018 v.367. https://doi.org/10.1016/j.jcat.2018.08.025.

(27) Kuai, L.; Chen, Z.; Liu, S.; Kan, E.; Yu, N.; Ren, Y.; Fang, C.; Li, X.; Li, Y.; Geng, B. Titania Supported Synergistic Palladium Single Atoms and Nanoparticles for Room Temperature Ketone and Aldehydes Hydrogenation. *Nat Commun* **2020**, *11* (1), 1–9.

(28) Tang, Y.; Asokan, C.; Xu, M.; Graham, G. W.; Pan, X.; Christopher, P.; Li, J.; Sautet, P. Rh Single Atoms on TiO2 Dynamically Respond to Reaction Conditions by Adapting Their Site. *Nat Commun* **2019**, *10* (1), 4488. https://doi.org/10.1038/s41467-019-12461-6.

(29) Zhang, J.; Alexandrova, A. N. The Golden Crown: A Single Au Atom That Boosts the CO Oxidation Catalyzed by a Palladium Cluster on Titania Surfaces. *J Phys Chem Lett* **2013**, *4* (14), 2250–2255. https://doi.org/10.1021/jz400981a.

(30) Zhou, X.; Hwang, I.; Tomanec, O.; Fehn, D.; Mazare, A.; Zboril, R.; Meyer, K.; Schmuki, P. Advanced Photocatalysts: Pinning Single Atom Co-Catalysts on Titania Nanotubes. *Adv Funct Mater* **2021**, *31* (30), 2102843.

(31) Thompson, C. B.; Liu, L.; Leshchev, D. S.; Hoffman, A. S.; Hong, J.; Bare, S. R.; Unocic, R. R.; Stavitski, E.; Xin, H.; Karim, A. M. CO Oxidation on Ir_1/TiO_2 : Resolving Ligand Dynamics and Elementary Reaction Steps. *ACS Catal* **2023**, *13* (12), 7802–7811. https://doi.org/10.1021/acscatal.3c01433.

(32) Lu, Y.; Thompson, C.; Kunwar, D.; Datye, A. K.; Karim, A. M. Origin of the High CO Oxidation Activity on CeO2 Supported Pt Nanoparticles: Weaker Binding of CO or Facile Oxygen Transfer from the Support? *ChemCatChem* **2020**, *12* (6), 1726–1733.

(33) Gänzler, A. M.; Casapu, M.; Doronkin, D. E.; Maurer, F.; Lott, P.; Glatzel, P.; Votsmeier, M.; Deutschmann, O.; Grunwaldt, J.-D. Unravelling the Different Reaction Pathways for Low Temperature CO Oxidation on Pt/CeO $_2$ and Pt/Al $_2$ O $_3$ by Spatially Resolved Structure–Activity Correlations. *J Phys Chem Lett* **2019**, *10* (24), 7698–7705. https://doi.org/10.1021/acs.jpclett.9b02768.

(34) Liu, L.; Thompson, C. B.; Mou, T.; Karim, A. M.; Xin, H. Elucidation of Site Structures and CO Oxidation Kinetics of the Ir1/TiO2 Single-Atom Catalyst. *Chem Catalysis* **2024**, 100900. https://doi.org/10.1016/j.checat.2024.100900.

(35) Scheiber, P.; Fidler, M.; Dulub, O.; Schmid, M.; Diebold, U.; Hou, W.; Aschauer, U.; Selloni, A. (Sub)Surface Mobility of Oxygen Vacancies at the <math Display="inline"> <msub> <mi>TiO</Mi> <mn>2</Mn> </Msub> </Math> Anatase (101) Surface. *Phys Rev Lett* **2012**, *109* (13), 136103. https://doi.org/10.1103/PhysRevLett.109.136103.

(36) He, Y.; Dulub, O.; Cheng, H.; Selloni, A.; Diebold, U. Evidence for the Predominance of Subsurface Defects on Reduced Anatase <math Display="inline"> <msub> <mi>TiO</Mi> <mn>2</Mn> </Msub> <mo Stretchy="false">(</Mo> <mn>101</Mn> <mo Stretchy="false">)</Mo> </Math>. *Phys Rev Lett* **2009**, *102* (10), 106105. https://doi.org/10.1103/PhysRevLett.102.106105.

(37) Ammal, S. C.; Heyden, A. Origin of the Unique Activity of Pt/TiO2 Catalysts for the Water–Gas Shift Reaction. *J Catal* **2013**, *306*, 78–90. https://doi.org/10.1016/j.jcat.2013.06.014.

(38) Aschauer, U.; He, Y.; Cheng, H.; Li, S.-C.; Diebold, U.; Selloni, A. Influence of Subsurface Defects on the Surface Reactivity of TiO $_2$: Water on Anatase (101). *The Journal of Physical Chemistry C* **2010**, *114* (2), 1278–1284. https://doi.org/10.1021/jp910492b.

(39) Hook, A.; Celik, F. E. Density Functional Theory Investigation of the Role of Cocatalytic Water in the Water Gas Shift Reaction over Anatase TiO $_2$ (101). *Ind Eng Chem Res* **2018**, *57* (20), 6830–6841. https://doi.org/10.1021/acs.iecr.8b00532.

(40) Cohen, A. J.; Mori-Sánchez, P.; Yang, W. Insights into Current Limitations of Density Functional Theory. *Science (1979)* **2008**, *321* (5890), 792–794. https://doi.org/10.1126/science.1158722.

(41) Mori-Sánchez, P.; Cohen, A. J.; Yang, W. Localization and Delocalization Errors in Density Functional Theory and Implications for Band-Gap Prediction. *Phys Rev Lett* **2008**, *100* (14), 146401. https://doi.org/10.1103/PhysRevLett.100.146401.

(42) Cohen, A. J.; Mori-Sánchez, P.; Yang, W. Fractional Charge Perspective on the Band Gap in Density-Functional Theory. *Phys Rev B* **2008**, *77* (11), 115123. https://doi.org/10.1103/PhysRevB.77.115123.

(43) T. Campbell, C. The Degree of Rate Control: A Powerful Tool for Catalysis Research. *ACS Catal* **2017**, *7* (4), 2770–2779. https://doi.org/10.1021/acscatal.7b00115.

(44) Motagamwala, A. H.; Dumesic, J. A. Microkinetic Modeling: A Tool for Rational Catalyst Design. *Chem Rev* **2021**, *121* (2), 1049–1076. https://doi.org/10.1021/acs.chemrev.0c00394.

(45) Campbell, C. T.; Mao, Z. Analysis and Prediction of Reaction Kinetics Using the Degree of Rate Control. *J Catal* **2021**, *404*, 647–660. https://doi.org/10.1016/j.jcat.2021.10.002.

(46) Sabbe, M. K.; Reyniers, M.-F.; Reuter, K. First-Principles Kinetic Modeling in Heterogeneous Catalysis: An Industrial Perspective on Best-Practice, Gaps and Needs. *Catal Sci Technol* **2012**, *2* (10), 2010. https://doi.org/10.1039/c2cy20261a.

(47) Guo, C.; Mao, Y.; Yao, Z.; Chen, J.; Hu, P. Examination of the Key Issues in Microkinetics: CO Oxidation on Rh(1 1 1). *J Catal* **2019**, *379*, 52–59. https://doi.org/10.1016/j.jcat.2019.09.012.

(48) Piccinin, S.; Stamatakis, M. Steady-State CO Oxidation on Pd(111): First-Principles Kinetic Monte Carlo Simulations and Microkinetic Analysis. *Top Catal* **2017**, *60* (1–2), 141–151. https://doi.org/10.1007/s11244-016-0725-5.

(49) Döpking, S.; Plaisance, C. P.; Strobusch, D.; Reuter, K.; Scheurer, C.; Matera, S. Addressing Global Uncertainty and Sensitivity in First-Principles Based Microkinetic Models by an Adaptive Sparse Grid Approach. *J Chem Phys* **2018**, *148* (3). https://doi.org/10.1063/1.5004770.

(50) Wang, L.; Deo, S.; Mukhopadhyay, A.; Pantelis, N. A.; Janik, M. J.; Rioux, R. M. Emergent Behavior in Oxidation Catalysis over Single-Atom Pd on a Reducible CeO $_2$ Support via Mixed Redox Cycles. *ACS Catal* **2022**, *12* (20), 12927–12941. https://doi.org/10.1021/acscatal.2c03194.

(51) Bhandari, S.; Rangarajan, S.; Maravelias, C. T.; Dumesic, J. A.; Mavrikakis, M. Reaction Mechanism of Vapor-Phase Formic Acid Decomposition over Platinum Catalysts: DFT, Reaction Kinetics Experiments, and Microkinetic Modeling. *ACS Catal* **2020**, *10* (7), 4112–4126. https://doi.org/10.1021/acscatal.9b05424.

(52) Yang, H. G.; Sun, C. H.; Qiao, S. Z.; Zou, J.; Liu, G.; Smith, S. C.; Cheng, H. M.; Lu, G. Q. Anatase TiO2 Single Crystals with a Large Percentage of Reactive Facets. *Nature* **2008**, *453* (7195), 638–641.

(53) Lazzeri, M.; Vittadini, A.; Selloni, A. Structure and Energetics of Stoichiometric TiO 2 Anatase Surfaces. *Phys Rev B* **2001**, *63* (15), 155409.

(54) Kresse, G.; Furthmüller, J. Efficiency of Ab-Initio Total Energy Calculations for Metals and Semiconductors Using a Plane-Wave Basis Set. *Comput Mater Sci* **1996**, *6* (1), 15–50. https://doi.org/https://doi.org/10.1016/0927-0256(96)00008-0.

(55) Kresse, G.; Furthmüller, J. Efficient Iterative Schemes for Ab Initio Total-Energy Calculations Using a Plane-Wave Basis Set. *Phys Rev B* **1996**, *54* (16), 11169–11186. https://doi.org/10.1103/PhysRevB.54.11169.

(56) Perdew, J. P.; Burke, K.; Ernzerhof, M. Generalized Gradient Approximation Made Simple. *Phys Rev Lett* **1996**, *77* (18), 3865–3868. https://doi.org/10.1103/PhysRevLett.77.3865.

(57) Steinmann, S. N.; Corminboeuf, C. A Generalized-Gradient Approximation Exchange Hole Model for Dispersion Coefficients. *J Chem Phys* **2011**, *134* (4), 044117. https://doi.org/10.1063/1.3545985.

(58) Steinmann, S. N.; Corminboeuf, C. Comprehensive Benchmarking of a Density-Dependent Dispersion Correction. *J Chem Theory Comput* **2011**. https://doi.org/10.1021/ct200602x.

(59) Blöchl, P. E. Projector Augmented-Wave Method. *Phys Rev B* **1994**, *50* (24), 17953–17979. https://doi.org/10.1103/PhysRevB.50.17953.

(60) Kresse, G.; Joubert, D. From Ultrasoft Pseudopotentials to the Projector Augmented-Wave Method. *Phys Rev B* **1999**, *59* (3), 1758–1775. https://doi.org/10.1103/PhysRevB.59.1758.

(61) Anisimov, V. I.; Aryasetiawan, F.; Lichtenstein, A. I. First-Principles Calculations of the Electronic Structure and Spectra of Strongly Correlated Systems: The **LDA** + *U* Method. *Journal of Physics: Condensed Matter* **1997**, *9* (4), 767–808. https://doi.org/10.1088/0953-8984/9/4/002.

(62) Dudarev, S.; Botton, G. Electron-Energy-Loss Spectra and the Structural Stability of Nickel Oxide: An LSDA+U Study. *Phys Rev B Condens Matter Mater Phys* **1998**. https://doi.org/10.1103/PhysRevB.57.1505.

(63) Morgan, B. J.; Watson, G. W. A DFT+U Description of Oxygen Vacancies at the TiO2 Rutile (110) Surface. *Surf Sci* **2007**, *601* (21), 5034–5041. https://doi.org/https://doi.org/10.1016/j.susc.2007.08.025.

(64) von Ahsen, B.; Wartchow, R.; Willner, H.; Jonas, V.; Aubke, F. Bis(Carbonyl)Platinum(II) Derivatives: Molecular Structure of Cis-Pt(CO)2(SO3F)2, Complete Vibrational Analysis of Cis-Pt(CO)2Cl2, and Attempted Synthesis of Cis-Pt(CO)2F2. *Inorg Chem* **2000**, *39* (20), 4424–4432. https://doi.org/10.1021/ic000280j.

(65) Phromma, S.; Wutikhun, T.; Kasamechonchung, P.; Eksangsri, T.; Sapcharoenkun, C. Effect of Calcination Temperature on Photocatalytic Activity of Synthesized TiO2

Nanoparticles via Wet Ball Milling Sol-Gel Method. *Applied Sciences* **2020**, *10* (3), 993. https://doi.org/10.3390/app10030993.

(66) Wetchakun, N.; Incessungvorn, B.; Wetchakun, K.; Phanichphant, S. Influence of Calcination Temperature on Anatase to Rutile Phase Transformation in TiO2 Nanoparticles Synthesized by the Modified Sol–Gel Method. *Mater Lett* **2012**, *82*, 195–198. https://doi.org/10.1016/j.matlet.2012.05.092.

(67) Oudenhuijzen, M. K.; Kooyman, P. J.; Tappel, B.; van Bokhoven, J. A.; Koningsberger, D. C. Understanding the Influence of the Pretreatment Procedure on Platinum Particle Size and Particle-Size Distribution for SiO2 Impregnated with [Pt2+(NH3)4](NO3−)2: A Combination of HRTEM, Mass Spectrometry, and Quick EXAFS. *J Catal* **2002**, *205* (1), 135–146. https://doi.org/10.1006/jcat.2001.3433.

(68) Kuo, C.-T.; Lu, Y.; Kovarik, L.; Engelhard, M.; Karim, A. M. Structure Sensitivity of Acetylene Semi-Hydrogenation on Pt Single Atoms and Subnanometer Clusters. *ACS Catal* **2019**, *9* (12), 11030–11041. https://doi.org/10.1021/acscatal.9b02840.

(69) Koros, R. M.; Nowak, E. J. A Diagnostic Test of the Kinetic Regime in a Packed Bed Reactor. *Chem Eng Sci* **1967**, *22* (3), 470. https://doi.org/10.1016/0009-2509(67)80134-9.

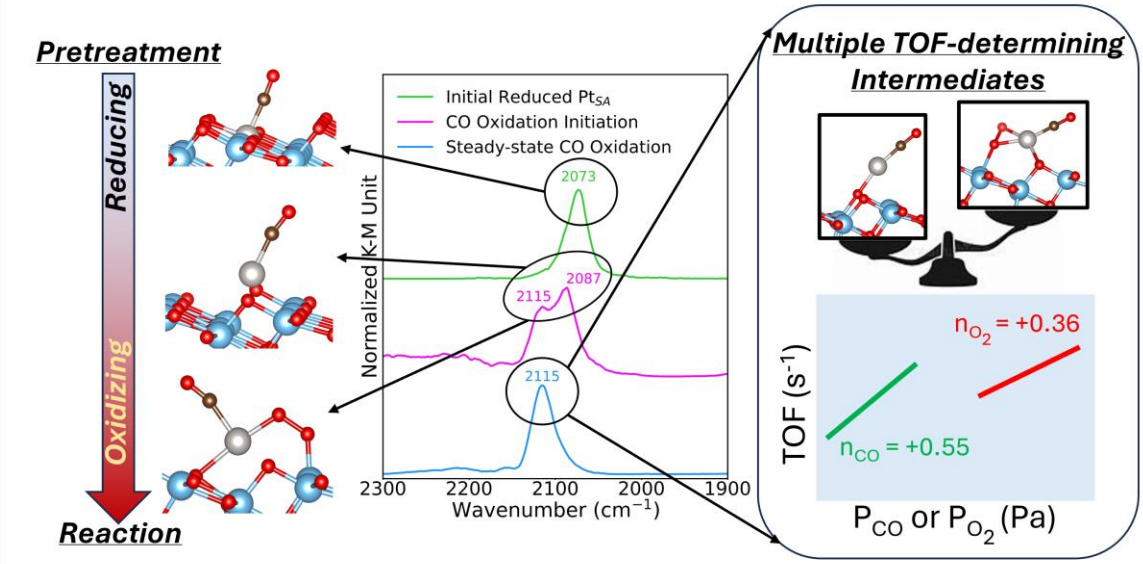
Pretreatment
Reducing
Oxidizing
Reaction
Initial Reduced Pt_{SA}
CO Oxidation Initiation
Steady-state CO Oxidation
2073
2087
2115
2115
Normalized K-M Unit
2300
2200
2100
2000
1900
Wavenumber (cm^{-1})
Multiple TOF-determining Intermediates
n_{O_2} = +0.36
n_{CO} = +0.55
TOF (s^{-1})
P_{CO} or P_{O_2} (Pa)

TOC graphic